# Proceedings of the ASME 2016 Conference on Smart Materials, Adaptive Structures and Intelligent Systems SMASIS2016 September 28-30, 2016, Stowe, VT, USA

### SMASIS2016-9071

#### **Alexander Pagano**

University of Illinois Urbana-Champaign Urbana, IL USA

#### Tongxi Yan

University of Illinois Urbana-Champaign Urbana, IL USA

#### **Brandon Leung**

MULTI-STABLE ORIGAMI STRUCTURE FOR CRAWLING LOCOMOTION

University of Illinois Urbana-Champaign Urbana, IL USA

#### A. Wissa

University of Illinois Urbana-Champaign Urbana, IL USA

#### **Brian Chien**

University of Illinois Urbana-Champaign Urbana, IL USA

#### S. Tawfick

University of Illinois Urbana-Champaign Urbana, IL USA

#### **ABSTRACT**

This paper presents the design of a bio-inspired crawling robot comprised of bi-stable origami building blocks. This origami structure, which is based on Kresling origami pattern, expands and contracts through coupled longitudinal and rotational motion similar to a screw. Controlled snapping, facilitated by buckling instability, allows for rapid actuation as seen in the mechanism of the hummingbird beaks or the Venus flytrap plant, which enables them to capture insects by fast closing actions. On a much smaller scale, a similar buckling instability actuates the fast turning motion of uni-flagellated bacteria. Origami provides a versatile and scale-free framework for the design and fabrication of smart actuators and structures based on this bi-stable actuation scheme. This paper demonstrates how a bi-stable origami structure, having the geometry of a polygonal base prism, can be used to actuate crawling gait locomotion. Bi-stable origami structures exhibit buckling instabilities associated with local bending and buckling of their flat panels. Traditional kinematic analysis of these structures based on rigid-plates and hinges at fold lines precludes the shape transformation readily observed in physical models. To capture this behavior, the model presented utilizes principles of virtual folding to analyze and predict the kinematics of the bistable origami building blocks. Virtual fold approximates panel bending by hinged, rigid panels, which facilitates the development of a kinematic solution via traditional rigid-plate analysis. As such, the kinetics and stability of the structures are investigated by assigning suitable torsional springs' constants to the fold lines. The results presented demonstrate the effect of fold-pattern geometries on the chirality (i.e. the rotational direction that results in expansion of the structure), and snapping behavior of the bi-stable origami structure. The crawling robot is presented as a case study for the use of this origami structure in various locomotion applications. The robot is comprised of two nested origami 'building blocks' with opposite chirality, such that their actuations are coupled rotationally. A servo motor is used to rotationally actuate the expansion and contraction of both the internal and external origami structures to achieve locomotion. Inclined barbs that extrude from the edges of the polygonal base engage with the ground surface, thus constraining the expansion or contraction to forward locomotion, as desired. The robot fabrication methods are presented and results from experiments performed on various surfaces are also discussed.

#### 1. INTRODUCTION

As autonomous systems are further integrated into everyday scenarios, there is a prevailing need to make these systems more adaptive, less obtrusive, and more independent. To address this need, we seek inspiration from natural systems which overcome an incredible variety of challenges with simple, adaptive solutions. For example, rapid motion of plants demonstrates how categorically slow moving systems have adaptively developed mechanisms that allow for fast motion [1]. Much of the motion in plants is hydraulically driven, nastic motion (there is no directional correlation between stimulus and response) which is controlled through differential internal cell (turgor) pressure [1]. The time limiting factor of such motion is the transport of water through the porous, elastic plant tissue which is largely affected by the length-scale of the desired motions [1]. This fundamental limitation for large, fast motion in plants can be overcome

through the coupling of mechanical instabilities and slow actuation over short length-scales.

Many diverse systems in nature depend on the controlled actuation of flexible structures through buckling instabilities for rapid motion in both predation and locomotion [2]-[4]. While buckling is typically associated with failure in mechanical systems, we've seen that the manipulation of bi-stable or multistable features allows for motion over large scales that would otherwise not be possible from other natural actuation schemes due to shortcomings in strength, speed or flexibility. For example, the snap-buckling associated with the rapid closure of Venus flytraps is due to the reconfiguration from convex to concave curvature of its leaves. This motion is driven by a controlled change in the principle curvature of the leaf through local variation in turgor pressure that, due to geometric constraints, is coupled to a stretching deformation mode that stores elastic energy. This coupling allows for small perturbations in curvature to result in large, rapid motion of the leaf [2]. A similar mechanism is used in the beaks of hummingbirds to produce a fast-closing action unattainable by direct muscular control. The pre-configuration of an anisotropically compliant bone in the hummingbird beak allows for smooth flexion to a strained position which can then be triggered to facilitate the fast expenditure of elastic energy as the beak snaps back to its closed equilibrium state [4]. Buckling instability has also been shown to be a dominant feature of locomotion for uni-flagellated bacteria, suggesting that the bistable actuation scheme is viable independent of scale [3]. In this paper, we utilize origami as a platform for the scale-free investigation of actuation based on the buckling instabilities of thin, flexible features.

The outstanding number of natural systems which utilize folding-in conjunction with the low material cost and theoretical freedom of 2D materials-identifies origami as a nearly barrier-free platform for biomimetic design. A wealth of useful systems is discovered when the conditions that result in natural folding are investigated. The folding mechanisms of pine-cones, hawkmoths, poppy petals, and horse-chestnut leaves have all resulted in useful origami structures, among which are the ubiquitous Miura-ori pattern [5] and the Kresling pattern [6] which is investigated here. These structures have broad-reaching applications in deployable and rigidizable systems as well as multi-functional systems providing both structure and actuation as discussed in the case study herein. Through the manipulation of "defect states" created by the buckling of thin sheets, origami also provides the framework for the development of reprogrammable, mechanical metamaterials [7]. Simplistic tools for the modeling of these structures such as rigid-panel analysis and the principles of virtual folds enable facile investigation of their properties so that the development of useful structures is straightforward [8].

The ability to produce a functional and geometrically complex 3D mechanical system from a flat sheet introduces exciting opportunities in the field of robotics for remote, autonomously deployable systems or low cost integrated locomotion. Self-folding origami robots have demonstrated the

viability of folded monolithic structures for a variety of tasks [9]–[11]. For example, Rus, Wood and co-workers demonstrated how self-assembly can be used to create a deployable robot that folds itself from a flat sheet and walks away [10] and the diversity of origami patterns which are useful for locomotion [9]. The reconfigurable nature of origami systems often allows for a multitude of potential functional folding schemes within a given structure. Moreover, in a monolithic system where load-bearing structure and locomotion are facilitated by the same components, this re-configurability lends itself to multi-model and multifunctional design. For example, the Tribot 'robogami' is capable of moving via both jumping and crawling locomotion by the same actuation mechanism [12] which provides more opportunities for success when navigating unpredictable terrains. Multi-functional design facilitated by folded structures has the potential to simplify robotics design through the integrated use of coupled structural and actuation mechanisms while decreasing both weight and fabrication costs.

In this study we demonstrate the design, analysis and fabrication of a bi-stable origami structure inspired by the Kresling pattern. Through the coupling of rotational and linear motion, this structure uses buckling instabilities to accomplish large-stroke snapping motion from relatively small inputs. We demonstrate the functional application of this mechanism in the case study with a crawling robot that utilizes monolithic, multifunctional design to realize locomotion from a single motor. The remainder of this paper is organized as follows: Section 2 presents the design and mechanics of the origami structures; Sections 3 and 4 detail the kinematics of the origami structure represented as rigid panels; Section 5 presents the crawling robot design and experimental results as a case study.

#### 2. DESIGN AND MECHANICS OF THE ORIGAMI

#### Geometric Description of the origami structure

The origami structure can be uniquely defined by the three parameters, n, R, and  $\lambda$ , which are the number of sides of the basal polygon, the circumradius of the basal polygon, and the angle ratio, respectively [13]. The angle ratio,  $\lambda$ , determines the aspect ratio of the structure and the degree of transformation during folding. From these parameters, the remaining fold lengths and angles are easily determined geometrically from the generic crease pattern (CP) (Fig. 1A) and basic polygon relations. The governing equations used to create the CP for a specific structure are given in Eqs. 1-3. The valley crease length, l, is determined through trigonometric analysis of the folded tower in the 'closed' position (Fig. 1C) so that all fold lines and vertices lie in the same plane (Eq. 4).

The construction of the structure from the flat CP (**Fig. 1A**) is accomplished by folding and rolling it into polygonal prism such that points A and B overlap with A\* and B\*, which results in the expanded or 'open' structure (**Fig. 1B**). When a force is applied on the top of the structure (while allowing free rotation), it contracts while exhibiting a snapping motion from the open to closed positions as demonstrated in **Fig. 2**. This transformation

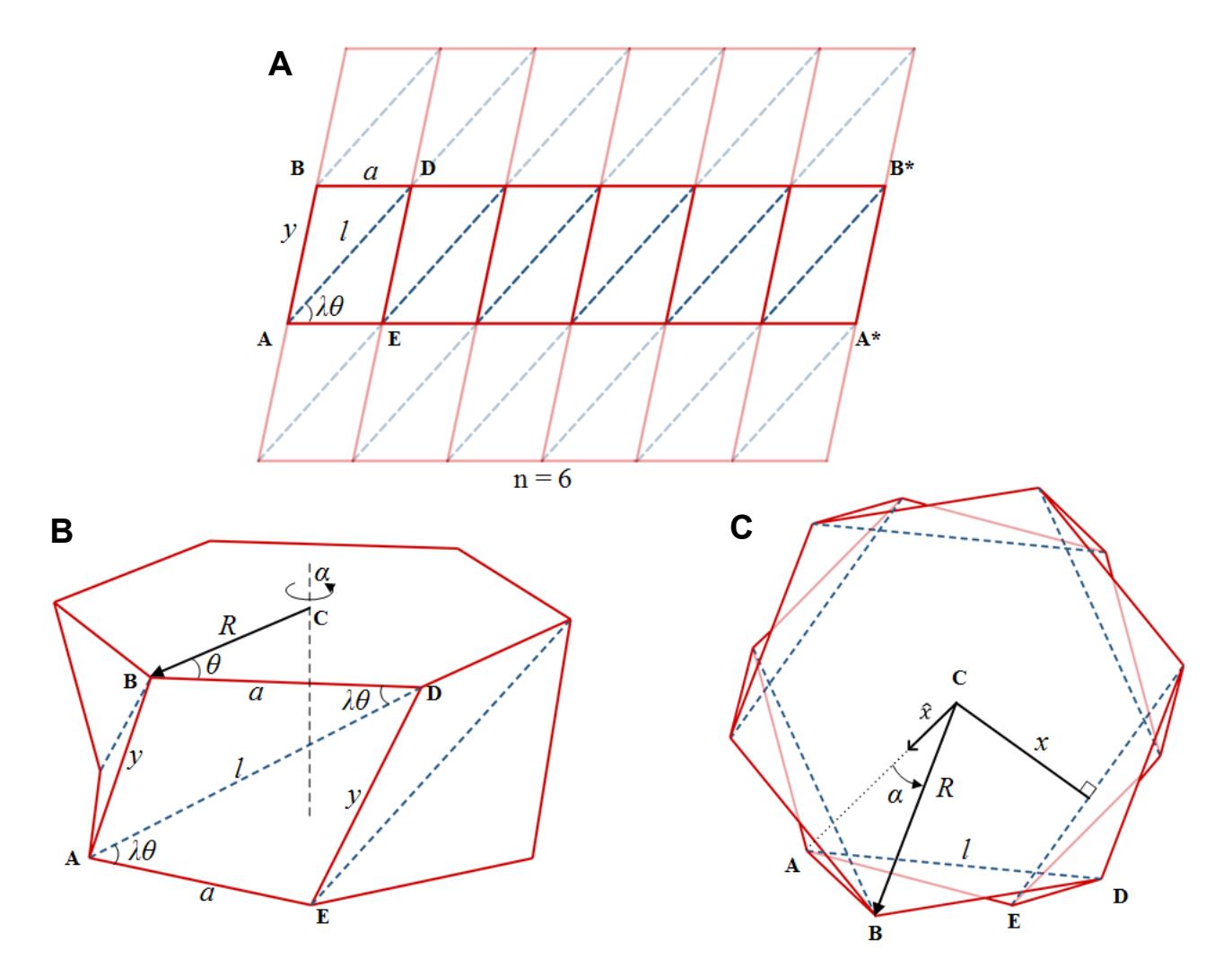


Fig. 1 – Geometry of the origami structure. A) The crease pattern (CP) for the polygonal prism origami structure shown in **B** which is derived from the Kresling Pattern [6]. Mountain folds are shown as solid, red lines and valley folds are shown in dashed blue. The schematics define the geometric parameters: n is the number of sides, a is the polygon side length, l is the diagonal valley-crease length, p is the side panel length, the angle  $\theta$  is half the internal angle of the basal polygon, and  $\lambda$ , the angle ratio, is a metric of transformation between open and closed states and can vary between 0.5 and 1 for the bistable behavior. **B**) A hexagonal-based Kresling origami is constructed from the shaded pattern in A where n=6 and  $\lambda=0.8$ . Variation in circumradius R results in scaling the size of this origami. Also shown is rotation angle,  $\alpha$ , for rotation of the top polygon about the dashed axis shown in **B**. **C**) Top down view of the structure shown in **B** while in its closed position. The crease length of the diagonal valley-fold, l, is determined trigonometrically from this schematic. The internal radius, x, of the cavity formed by the valley-folds while in the closed position is also determined from this view. The rotation angle is measured from the x-axis to the vector R as shown. The x-axis is chosen to intersect the first vertex of the bottom polygon, labeled A.

is non-rigid in that, in addition to the local folding of the mountain and valley crease lines, elastic deformation of the flat panels is required to complete the transformation. For simplicity in discussion we will refer to the transition from open to closed positions as 'contraction' and the inverse transformation from closed to open 'expansion'. Depending on the value of  $\lambda$ , when the origami is fully folded, an internal cavity is formed with some internal radius, x. This internal radius is characteristic of the polygon formed by the valley folds when in the closed position, and is determined trigonometrically from the same closed configuration used to determine the crease length, l (Eq. 5, see Fig. 1C). The cavity allows for the concentric placement of two

origami structures so that one rests in the cavity of the other without interference during expansion and contraction as demonstrated in the case study, described in Section 5. The geometric relations describing the origami are listed in Eq. 1-5.

$$a = 2R\sin\left(\frac{\pi}{n}\right) \tag{1}$$

$$y = (l^2 + a^2 - 2la\cos(\lambda\theta))^{1/2}$$
 (2)

$$\theta = \frac{\pi(n-2)}{2n} \tag{3}$$

$$l = 2R\cos(\theta(1-\lambda)) \tag{4}$$

$$x = R\sin(\theta(1-\lambda)) \tag{5}$$

When the origami is constructed from the CP into the open position (**Fig. 1B**), its configuration is expressed by its height, H, and the rotation angle,  $\alpha$ , which describes the rotation of the top polygon with respect to a frame fixed to the bottom polygon. The chirality of the structure, defined here as the direction of rotation,  $\alpha$ , which results in expansion of the structure, can be changed by taking the mirror image of the CP in **Fig. 1A** reflected about a vertical axis. The origami structure shown in **Fig. 1B** has negative chirality but positive and negative chirality are mathematically indistinguishable when considering the behavior of the structure during expansion or contraction.

#### Foldability Analysis for rigid origami

The CP for a single origami building block shown in **Fig. 1A** is comprised of one row of n parallelogram panels. This CP is rigid foldable, which indicates that the polygonal prism can be constructed from a flat CP by simply bending the fold lines without deforming the flat panels. This rigid foldability can be confirmed by analyzing the number of degrees of freedom (DOF) for the CP,

$$DOF = N - 3 \tag{6}$$

where N is the number of mountain or valley folds that meet at a vertex [14]. To construct a single unit cell (one row from **Fig. 1A**), 4 fold lines intersect at vertex D: the two horizontal

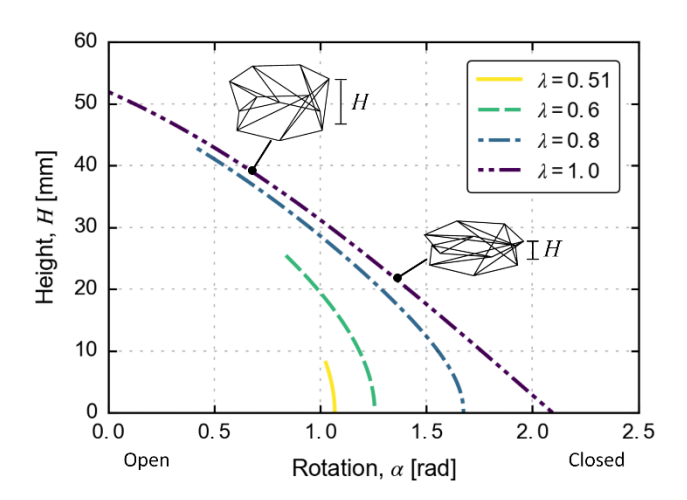
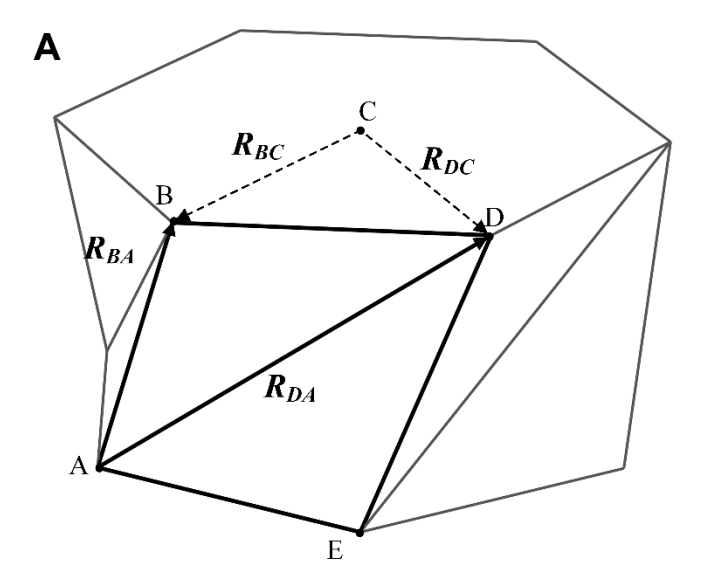


Fig. 2 – Change in origami height, H, calculated as a function of rotation angle,  $\alpha$ , to demonstrate contraction of the origami. Height is plotted for values of angle ratio,  $\lambda$ , spanning its range of  $0.5 < \lambda \le 1.0$  to demonstrate the effect of  $\lambda$  on the extent of transformation during contraction. Note that as  $\lambda$  approaches 0.5, origami height and rotation vary less between initial (open) and final (closed) states than for larger values of  $\lambda$ .

mountain-folds labeled a, the diagonal mountain-fold, y, and the diagonal valley-fold, l. Therefore each vertex of the CP has 1 DOF and the prism construction is rigidly foldable [14]. Following the creasing of mountain and valley folds, the vertices corresponding to the 1<sup>st</sup> and  $n^{th}$  panel (for example A,B and A\*,B\* in **Fig. 1A**) are overlapped to create the basal polygon. Notably,



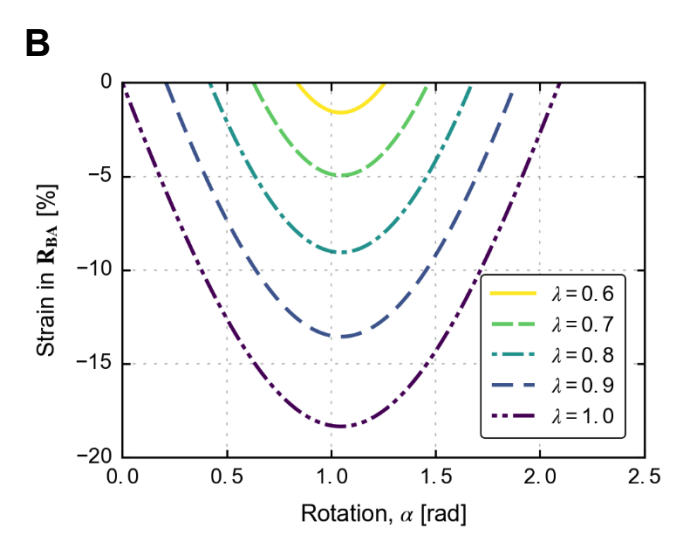


Fig. 3 – A) The origami structure shown in the open position, where the vertices and representative vectors used in the vector loop equation are shown. The thick black lines represent the  $n^{th}$  panel, of which the triangular 'unit cell'  $\overline{ABD}$  is sufficient to determine the motion of the structure during contraction or expansion. All other positions can be determined through arbitrary rotations. The structure shown represents R = 30 mm,  $\lambda = 0.8$  and n = 6. B) Theoretical strain in vector  $R_{BA}$  as a function of rotation is plotted here for several values of angle ratio,  $\lambda$ , to demonstrate the effect of  $\lambda$  on the bistable behavior of the tower. Theoretical strain is given here as a metric for the extent of deformation required for expansion or contraction of the structure between kinematically allowable open and closed positions. As the angle ratio,  $\lambda$ , increases, the theoretical strain increases so that more deformation is required for higher values of angle ratio.

for  $\lambda$ >0.5, the overlap can be done in such a way to construct an expanded polygonal prism or a flat polygon (inset **Fig. 2**). Once the vertices are fixed to one another (e.g. by gluing), the formed origami structure is kinematically rigid in both of these configurations. This additional constraint, created by gluing the vertices, fully defines the position of each vertex with respect to its neighbor so that the structure no longer has available degrees of freedom. In other words, if the panels are truly rigid, the expanded polygonal prism having  $\lambda$ >0.5 cannot be contracted and vice versa. If the panels are bendable, the polygonal prism exhibits snapping between the expanded and contracted configurations. However, it is not readily apparent from the CP what the values of height, H, and rotation,  $\alpha$ , are at these positions.

## 3. KINEMATIC ANALYSIS OF RIGID PANELS AND FOLDING JOINTS

To determine the configuration of the folded origami structure, a vector loop equation for the closed loop,  $R_{BA}$ ,  $R_{BC}$ ,  $R_{DC}$ ,  $R_{DA}$ , was solved numerically using a custom Python program.

$$R_{BA} - R_{BC} + R_{DC} - R_{DA} = 0 (7)$$

$$\mathbf{R}_{BA} = R(-1 + \cos \alpha)\hat{x} + R\sin \alpha \,\hat{y} + H\,\hat{z} \tag{8}$$

$$\mathbf{R}_{BC} = R\cos\alpha\,\hat{x} + R\sin\alpha\,\hat{y} + 0\,\hat{z} \tag{9}$$

$$\mathbf{R_{DC}} = R\cos\left(\alpha + \frac{2\pi}{n}\right)\hat{x} + R\sin\left(\alpha + \frac{2\pi}{n}\right)\hat{y} + 0\,\hat{z} \tag{10}$$

$$\mathbf{R}_{DA} = R\left(-1 + \cos\left(\alpha + \frac{2\pi}{n}\right)\hat{x} + R\sin\left(\alpha + \frac{2\pi}{n}\right)\hat{y} + \theta\hat{z}\right) + H\hat{z}$$

$$(10)$$

$$+ H\hat{z}$$

The following constraints were used to attain the numerical solution for height and rotation in the initial position, i.e. open:

1) The angle between vectors  $\mathbf{R}_{BD}$  and  $\mathbf{R}_{DA}$  is  $\lambda \theta$ 

$$\mathbf{R}_{\mathbf{R}\mathbf{D}} \cdot \mathbf{R}_{\mathbf{D}\mathbf{A}} = (l \times a) \cos(\lambda \theta) \tag{12}$$

2) The fold  $\overline{AD}$  is a rigid line represented by a vector  $R_{DA}$  with magnitude l

$$\|\mathbf{R}_{\mathbf{D}\mathbf{A}}\| = l \tag{13}$$

Using the Newton-Raphson method, the constraint equations are numerically solved by systemically varying the components of the vector loop vectors until the correct solution was found. In this way, the initial rotation angle was determined by solving the first constraint, which was then used in conjunction with the second constraint to determine the structure's initial height. Once the open configuration was defined, the final rotation was determined geometrically from the closed position where H=0 by definition. As previously stated, folding from the open to closed position requires some non-rigid deformation of the CP. To investigate the behavior of the structure during expansion and contraction we mathematically

allowed the length of vector  $R_{BA}$  (equivalent to  $R_{DE}$ ) to vary throughout folding. This introduces an additional degree of freedom that allows the model to smoothly transition from open to closed positions, thus conceptually simplifying the expression of deformation to a single dimension. Contraction was then simulated by stepping from initial to final rotation angles with equal step size. Height was then determined at each rotational step to fully define the configuration of the structure during expansion or contraction. The parameter of 'rotation' was specifically chosen as the input here since it is a relevant input for the motor-driven locomotion of the case study.

The degree of deformation required for folding, which, as discussed later, is a direct measure of the bistability of the system, can then be quantified by calculating the theoretical change in free length  $R_{BA}$  (**Fig. 3**). This additional degree of freedom is realized in physical paper models through the use of relief cuts along folds  $\overline{AB}$ . These cuts allow the length of  $R_{BA}$  to vary through the bending of adjacent panels so that corners A and B contract in the z-direction. This bending describes the motion of physical models better than simply strained links and can be modeled as the bending of the triangular panels  $\overline{ABD}$  and  $\overline{AED}$  on either side of the diagonal valley-fold  $\overline{AD}$ .

#### 4. KINEMATIC ANALYSIS INCLUDING VIRTUAL FOLDS

To account for panel bending, a "virtual fold" can be mathematically created between 2 vertices across a bending panel [8], [15]. Virtual fold assumes that mathematical fold lines can be added to represent the "hidden" degrees of freedom associated with the out of plane bending modes in kinematically rigid panels. To capture the bending behavior observed experimentally, virtual folds are placed along  $R_{FD}$  and  $R_{AF}$  for each panel as shown in Fig. 4. In this way, each panel was divided into triangular facets  $\overline{AFD}$ ,  $\overline{BFD}$ ,  $\overline{AF'D}$ , and  $\overline{AF'E}$  whose surface normals are parallel when panels are flat (i.e. open and closed configurations, Fig. 2) and have a non-zero scalar product during bending (Fig. 5). Triangular facets  $\overline{AF'D}$  and  $\overline{AF'E}$  can be represented as rotations of facets  $\overline{AFD}$  and  $\overline{BFD}$  and are therefore mathematically redundant. To simplify this discussion we will only consider the bending of virtual fold  $\overline{FD}$ .

The position of the virtual fold was chosen to emulate the conditions observed in physical models, but could be given any arbitrary position. At each step during contraction, the vertex of the virtual fold line which lies at point D on the top polygon remains fixed, while vertex at F is free to move according to the following constraints:

 The sides of the virtual facets must sum to the crease length, y, as defined in the CP (Fig. 1A) and Eq. 2. Each side has fixed length according to the rigid-panel assumption.

$$\|\mathbf{R}_{FA} + \mathbf{R}_{BF}\| = y \tag{14}$$

2) The virtual fold length is fixed throughout contraction. This fold length,  $l_d$ , is determined from the open configuration (**Fig. 3A**)

$$\|\mathbf{R}_{\mathbf{DF}}\| = l_d \tag{15}$$

3) The extent of out of plane deflection is determined trigonometrically from triangle  $\overline{ABF}$  where the change in length  $R_{BA}$  is given by the strain (**Fig. 3B**) while the lengths of  $R_{BF}$  and  $R_{FA}$  are fixed.

These constraint equations were numerically solved using the Newton-Raphson method as before. This allows for the position of each vertex to be determined at every step of expansion or contraction. From this, the fold angles can be determined by the scalar product of the surface normals of each facet (Fig. 5).

For the  $n^{\text{th}}$  panel of an n-sided polygonal prism represented as  $\overline{ABDE}$  we need only consider the fold angles of the folds,  $\overline{BD}$ ,  $\overline{FD}$  and  $\overline{AD}$  to characterize the entire structure since all other folds are rotationally symmetric. To analyze the potential energy associated with the origami snapping motion, torsional springs can be attached to the virtual fold lines to calculate the restoring force resulting from the bending of each triangular panel. This kinetic treatment is used to investigate the bistability of the structure.

#### Analysis of the Origami Bistability

By treating fold lines as torsional springs where the crease lines given by the CP have a different spring constant than the virtual folds which approximate panel bending, all of the material properties can be condensed into a single non-dimensional parameter, namely the fold stiffness ratio, which is the ratio of torsional spring constants associated with virtual folds and creases ( $k_b$  and  $k_c$  respectively). These spring constants can be experimentally measured. For the results presented here, the torsional spring constants determined experimentally by Silverberg *et al.* for 120 lb paper were used. These value were  $k_c = 170 \pm 20 \, mN \, m/rad$  for creases and  $k_b = 6 \, N \, m/rad$  for virtual folds [8].

The development of elastic energy during expansion or contraction as determined through the use of virtual folds and appropriate torsional springs can then be used to study the bistability of folded origami structures. The fold energy is given by the product of torsional spring potential and the length of the fold. For each fold, the associated folding energy is calculated and summed according to Eq. 16. The equilibrium position for the torsional spring potential is assumed to be the open configuration, and is represented by the subscript 0. The total elastic energy of the origami structure is determined from Eq. 16 and plotted as a function of rotation in Fig. 6 to investigate the bistability of the structure during expansion and contraction.

$$U_{total} = \frac{k_c}{2} \sum_{i=1}^{n} 2a (\theta_{BD,i} - \theta_{BD,0})^2 + l(\theta_{AD,i} - \theta_{AD,0})^2 + \frac{k_b}{2} \sum_{i=1}^{n} 2l_d \psi_{FD,i}^2$$
(16)

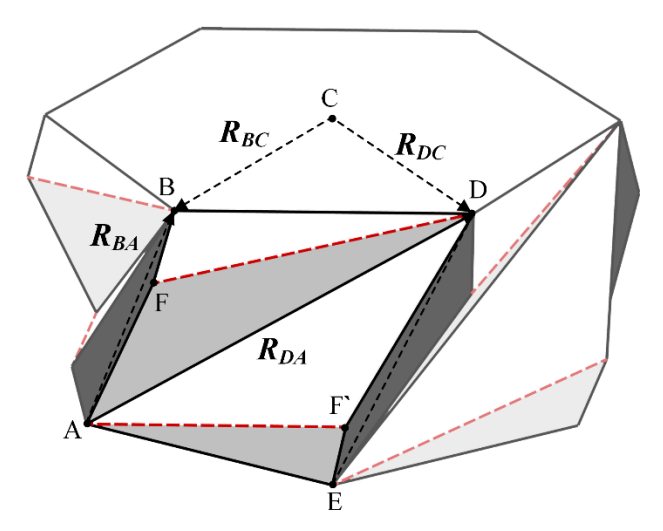
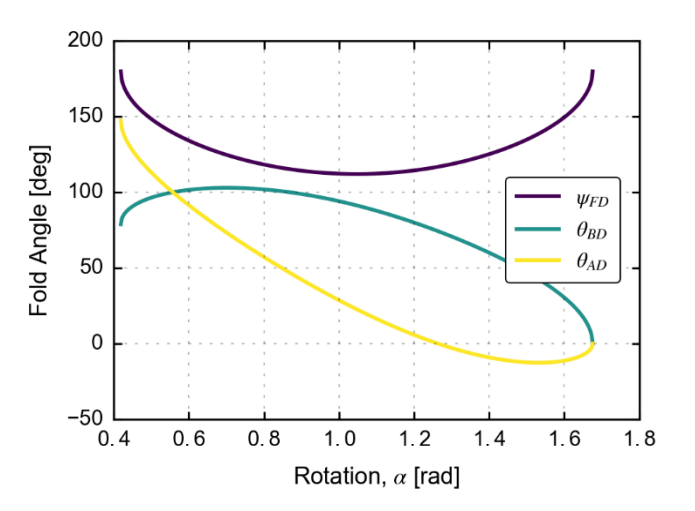


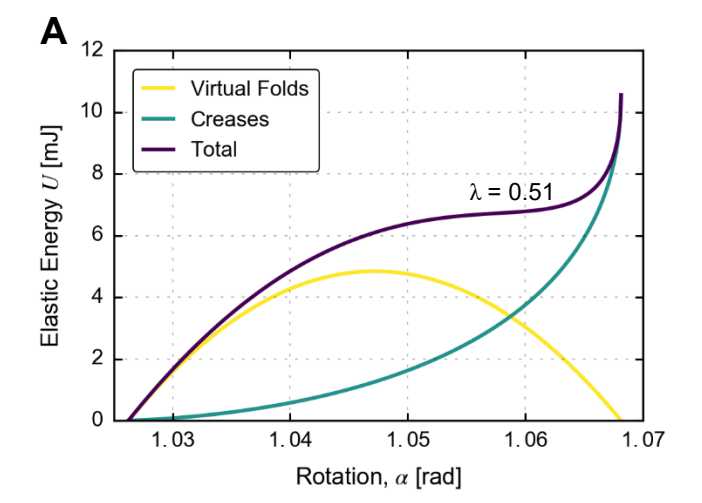
Fig. 4 – Accounting for panel bending by introducing virtual folds. During contraction, deformation is facilitated by out-of-plane bending of the triangular panels  $\overline{ABD}$  and  $\overline{AED}$ . The bending of these panels is treated rigidly through the introduction of virtual folding lines along  $\overline{FD}$  and  $\overline{AF'}$ .



**Fig. 5** — Characteristic fold angles as a function of rotation, determined from the scalar product of their respective surface normal vectors. Fold angles can be considered the angle between the facets on either side of the fold line. The fold angle,  $\psi_{FD}$ , corresponds to virtual fold lines  $\overline{FD}$  and  $\overline{AF'}$ . The virtual fold angle is initially and terminally 180 degrees due to the unbent structure in the open and closed configurations. The fold angles  $\theta_{BD}$  and  $\theta_{AD}$  of creases  $\overline{BD}$  (same as  $\overline{AE}$ ) and  $\overline{AD}$  take their initial values due to the geometric constraints of the structure in the open configuration. The negative angles are caused by the intersection of virtual facets.

The results from Eq. 16 are shown in Fig. 6. The origami structures have a maximum potential energy at a certain rotation angle which corresponds to the snapping motion. The bistability is more pronounced for higher aspect ratio polygonal prisms (defined by larger  $\lambda$  values). Importantly, since the deformations that occur are elastic, the system is able to repeatedly move from one kinematical configuration to another through bi-stable

snapping motion. In physical models, the thickness of folded layers prevents the system from accessing its co-planar, closed configuration. Instead, a force balance is established resulting in an equilibrium position at some nonzero height that can be conceptually correlated to the closed configuration of the structure. For the structure to be bi-stable, the elastic energy of the open and closed equilibrium configurations must be minimum energy states of the transformation. The energy required to produce the kinematically necessary deformations (i.e. panel bending) is then the barrier energy that separates the two equilibrium positions. It can be seen from **Fig. 6A** that bi-stable behavior begins to occur at low values of  $\lambda$  near its minimum of 0.5. However as  $\lambda$  increases to its maximum, more



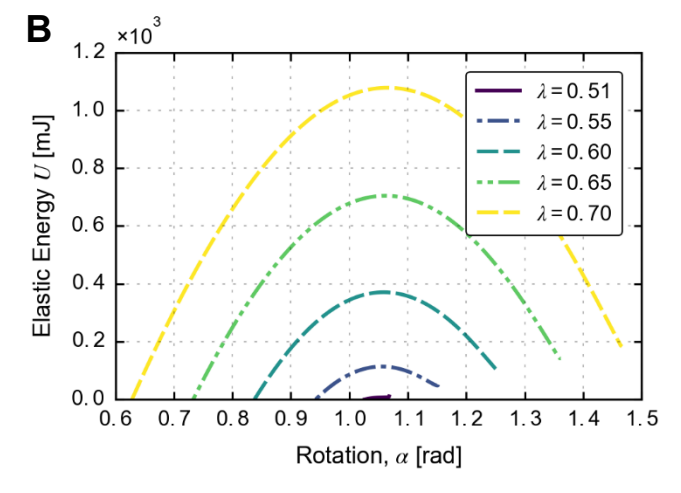


**Fig. 6** – **A)** Elastic energy contributions from creased folds and virtual folds are plotted as a function of energy. The total elastic energy associated with folding, as determined by **Eq. 16**, is also shown. In this case,  $\lambda$  is set equal to 0.51, and the ratio of  $k_b/k_c$  leads to an origami structure stable only in the expanded state. Here rotation angle increase corresponds to contraction of the origami, and creased lines have folding energies that are zero when in the open configuration. **B)** The total elastic energy from **Eq. 16** is plotted as a function of rotation to demonstrate that bi-stability is more pronounced for larger angle ratios.

deformation is required and therefore the behavior is increasingly bi-stable. The onset of bistability is a function of the fold stiffness ratio and the origami structure parameters n, R, and  $\lambda$ . Since the material properties dictate the fold stiffness ratio and we are free to specify the structure parameters to fit our purposes, this structure serves as a tunable bi-stable system created from a flat sheet.

The energy as a function of rotation can then be used to determine the torque associated with holding the structure in a certain configuration. This was accomplished using the force energy relation in Eq. 17. The work required for each rotational step is then given by Eq. 18. This can then be related to the rotational and linear stiffness of the structure by Eqs. 19 and 20.

$$\tau = -\frac{\partial U}{\partial \alpha} \tag{17}$$

$$W = \tau \Delta \alpha \tag{18}$$

$$K_{rotational} = \frac{2W}{(\Delta \alpha)^2} \tag{19}$$

$$K_{linear} = \frac{2W}{(\Delta H)^2} \tag{20}$$

The rotational and linear stiffness of the structure during contraction are shown in **Fig. 7**. Regions of negative stiffness demonstrate the bistability of the structure, where a small perturbation carries the structure through a large displacement.

In summary, this origami pattern, based on the Kresling pattern, demonstrates bi-stable expansion and contraction facilitated by the buckling of thin panels. This structure can be uniquely specified by the three parameters n, R and  $\lambda$  which are respectively the number of sides of the basal polygon, the circumradius of the basal polygon and the angle ratio. Through these parameters and the selection of the fold stiffness ratio by

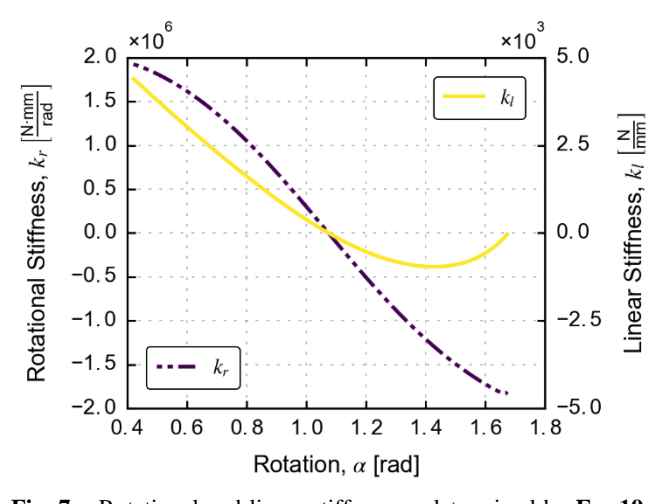


Fig. 7 – Rotational and linear stiffness as determined by Eq. 19 and Eq. 20 plotted as a function of rotation. The dashed line shows rotational stiffness and is plotted on the left axis (scaled by  $10^6$ ) while the solid line shows linear stiffness and is plotted on the right axis (scaled by  $10^3$ ). The upwards hook in linear stiffness is caused by the residual restoring force in the creased fold-lines.

material choice, the folding behavior of the structure can be fully determined and exploited. As a demonstrative example of the applications of this structure, we present a case study wherein this origami pattern is used for both structure and locomotion of a crawling robot.

#### 5. CASE STUDY: CRAWLING ROBOT

#### **Bio-Inspired Robot for Crawling Locomotion**

The bi-stable origami structure previously discussed is used as a 'building block' to construct a simple robot with crawling gait locomotion. The robot is assembled from two nested stacks of origami 'building blocks' with opposite chirality, such that the rotation of internal structure with respect to the external one causes expansion or contraction of the assembly. These building blocks are stacked concentrically as shown in Fig. 8A so that the internal and external structures are free to rotate coaxially without interference. This is ensured by choosing the values of n, R and  $\lambda$  for each structure so that the internal radius of the external structure, x, is greater than the circumradius of the internal structure (see Fig. 1). The anterior ends (furthest from the servo) of each tower are fixed to each other with a torquelimited coupling which allows for the expansion of the internal origami without risking damage due to over-rotation. On the posterior polygon of the external tower, a servo motor is mounted whose horn is fixed to the internal tower. Positive rotation of this servo horn results in the expansion of the internal tower, while the reaction torque on the external tower aids in this expansion due to their opposite chirality. Rotational actuation enables the controlled snapping of the internal origami which allows it to act as a telescopic boom which extends and contracts the outer origami. The internal origami structure is chosen to exhibit pronounced bi-stability through the selection of a high angle ratio ( $\lambda \ge 0.8$ ), while the external tower has a lower angle ratio  $(\lambda = 0.6)$  so it has a smoother transition between open and closed positions.

The expansion and contraction induces forward motion resembling the peristaltic locomotion of an earthworm, however, for this structure, linear expansion is not accompanied by a radial contraction as seen in peristalsis. Since the radius is constant during expansion, additional structures can be added to the origami towers to facilitate the appropriate weight distribution for crawling locomotion without changing the motion of the towers. To realize rotational actuation, a continuous rotation servo motor, servo motor holder, and servo horn adapter were fixed to the posterior end, which necessitated additional structures on the anterior end for balance (see Fig. 8). Weight holders were attached to each side so ball bearings, acting as counter weights, could be added as needed. A servo controller is used to control the angular displacement of the servo horn as well as the rotational speed. The total amount of rotation required to fully expand the structure is a function of the origami parameters, n, R, and  $\lambda$ , as well as the number of blocks in the internal and external towers. For the robots shown in Fig. 9, more than one revolution is required for the full expansion of the structure, therefore a continuous rotation servo was required for complete

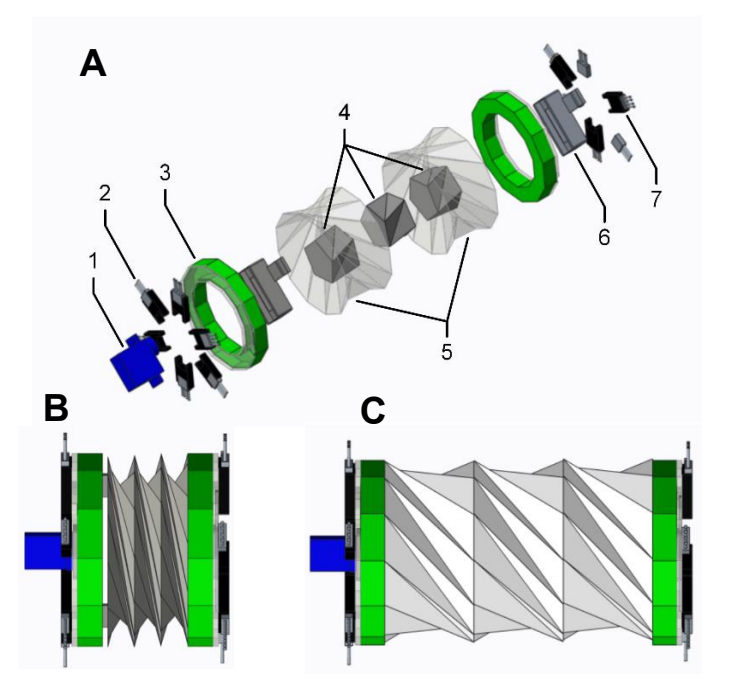


**Fig. 8** – **A**) Exploded isometric view of CAD model of robot prototype with components labeled: 1) Servo motor, 2) Barbs, 3) Weight holder, 4) Internal origami blocks, 5) External origami blocks, 6) Counterweight, 7) Bard holder **B**) CAD model showing robot in contracted/closed state **C**) CAD model showing robot in expanded/open state.

actuation. The controller was used to manually expand and contract the structure between the open (Fig. 9D&F) and closed (Fig. 9E&G) positions.

Barbs were used to systematically constrain the anterior and posterior ends of the robot during expansion and contraction to gain forward locomotion. These barbs were fabricated from 24gauge stainless steel wire and paper. SIM card holders were used as barb housings to enable the quick change of barb designs to test different orientations. Barb tips were bent towards the posterior end—opposite the direction of motion—to only allow for forward motion and prevent sliding backwards (see Fig. 9). In this case study, the robot prototype was tested with different barb configuration on various surfaces to determine the optimal condition for locomotion. The three configurations tested were the following: robot with no barbed feet, barbed feet at every other edge, and barbed feet at every edge (as pictured in Fig. 9A). The test surfaces included a smooth table top surface, a plywood surface, and a coarse sandpaper surface. It was shown that regardless of surface, the prototype with no barbed feet did not demonstrate forward motion and instead, expanded and contracted in a stationary position. However, the use of barbs facilitated forward motion by providing sufficient unidirectional friction for the expansion to cause the anterior end to slip while the posterior end remained fixed. When the test surface was too rough (i.e. the coarse sandpaper), the barbs were not able to sufficiently overcome the frictional forces regardless of configuration, and travel was limited. It was found that the

highest net forward displacement was on the plywood surface with the robot configured with barbs at every other edge. Testing was done using the paper origami robot prototype shown in Fig. 9A, B, D, and E. This robot is 9 cm long when fully contracted (Fig. 9E) and 16 cm long when fully expanded (Fig. 9D). The ideal gait would result in displacement equaling the difference between open and closed states so that all expansion results in forward progress. For this robot prototype, the maximum theoretical displacement per cycle would be 7 cm. Under the optimal testing conditions, the robot crawled forward 12.7 centimeters in three servo control cycles (open and close 3 times each) or 4.23 cm per cycle corresponding to an efficiency of 60%.

While inexpensive and readily available, paper doesn't offer the functional lifespan desired in most robotics applications. Additional prototypes were fabricated with more robust materials to withstand more cycles before failure. These prototypes were created from layers of cellulose acetate and natural rubber latex film. Cellulose acetate sheets were taped to a cardboard support, then laser cut according to the pattern derived from the origami crease pattern (Fig. 10A). Top and bottom polygons should also be laser cut, though a thicker material may be desired to provide sufficient rigidity. Natural rubber latex film was then glued to the cut acetate sheet, taking care to avoid bubbles under the latex layer. Using the polygons, the acetate and latex panels were then rolled and glued to the top and bottom as shown in Fig. 10B. The resulting building block (Fig. 10C) can then be stacked and glued to form the origami structures as desired. The newly fabricated robot will be tested to compare its performance to the paper-based robot.

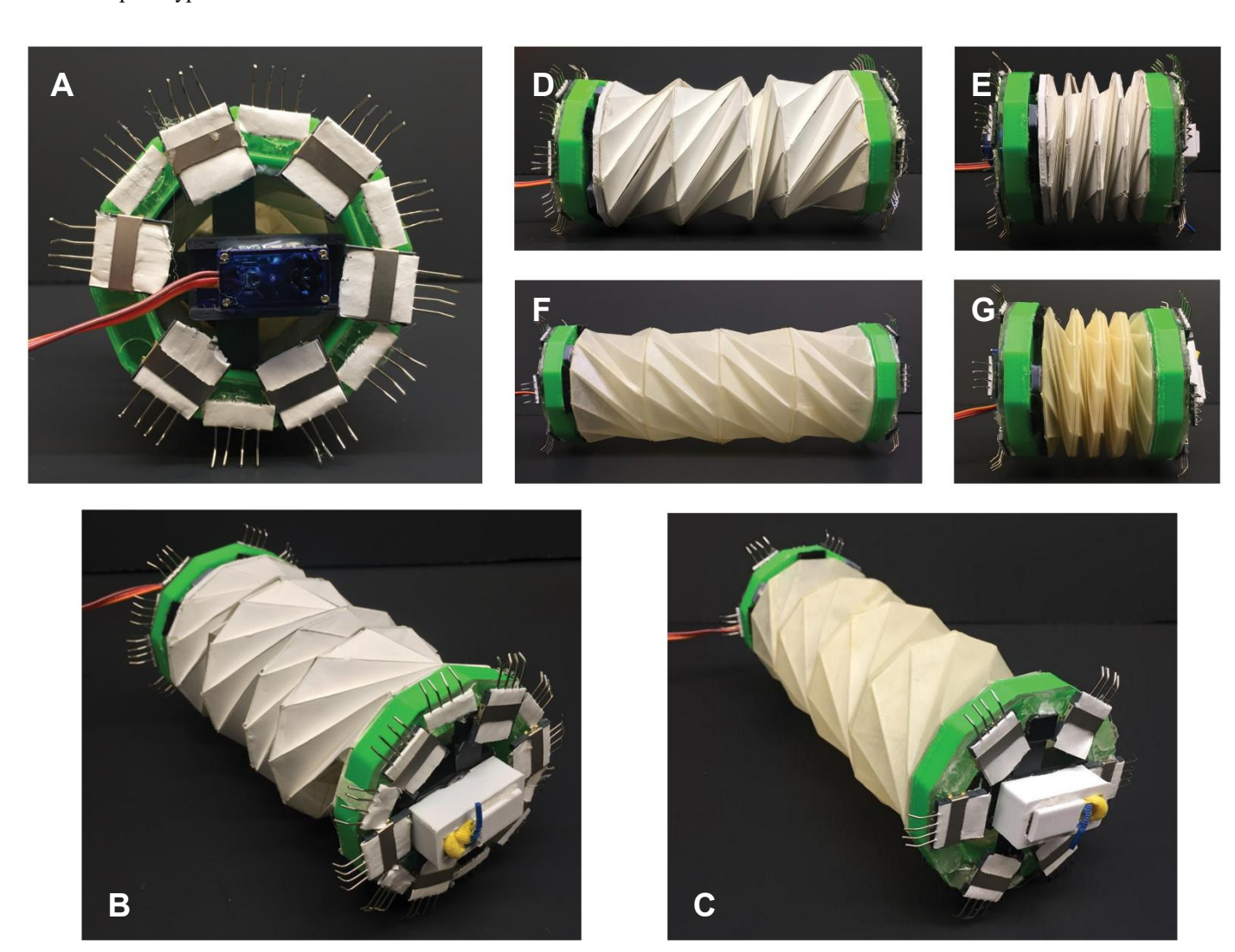


**Fig. 9** –  $\bf A$ ) Robot prototype posterior side. Showing servo mounting and barb configuration.  $\bf B$ ) Paper origami robot prototype fully assembled  $\bf C$ ) Cellulose Acetate + Latex origami robot prototype fully assembled  $\bf D$ ) Paper origami robot prototype in open position  $\bf E$ ) Paper origami robot prototype in closed position  $\bf F$ ) Acetate and Latex origami robot prototype in open position  $\bf G$ ) Acetate and Latex origami robot prototype in closed position

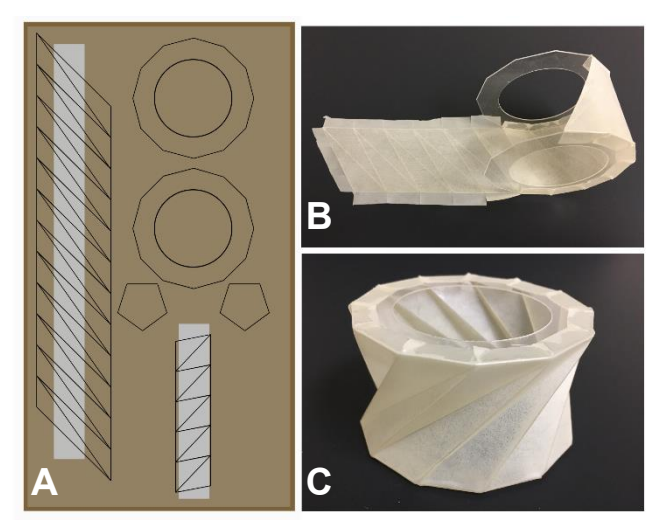


**Fig. 10** - **A**) Cellulose acetate sheet is taped to cardboard then laser-cut to produce "fold lines". **B**) Latex film is glued to acetate sheet and the structure is rolled and fixed to the top and bottom polygons **C**) The resulting latex and acetate structure can fold without relief cuts

#### SUMMARY

This manuscript presented the design and analysis of a bistable origami structure and its use in actuating a crawling robot gait. We presented the full analysis of the kinematics of the origami structure, as well as the potential energy evolution associated with its bi-stable snapping motion. This was achieved by applying the concept of virtual folds to account for panel bending. A simple application of the origami structure was realized through creating a crawling gate by concentrically nesting two origami structures with opposite chirality. The origami structures were actuated with a servo motor. Forward motion was achieved by adding inclined barbs on the circumference of the robot body to break the symmetry and ensure positive forward displacement and rotation. Due to backward slip, the gait achieved was 60% of the theoretical maximum. Further optimization of the friction interaction between the origami and the ground will enhance the gait quality. Future work will include additional consideration of the reconfigurability of this structure to realize multiple gaits from the same design as well as further studies of the latex and cellulose acetate prototypes.

#### **ACKNOWLEDGMENTS**

The authors acknowledge support from the Mechanical Science and Engineering at the University of Illinois Urbana-Champaign through start-up funding.

#### **REFERENCES**

- [1] J. M. Skotheim and L. Mahadevan, "Physical limits and design principles for plant and fungal movements.," *Science*, vol. 308, no. May, pp. 1308–1310, 2005.
- [2] Y. Forterre, J. M. Skotheim, J. Dumais, and L.

- Mahadevan, "How the Venus flytrap snaps," *Nature*, vol. 433, no. January, pp. 421–426, 2005.
- [3] K. Son, J. S. Guasto, and R. Stocker, "Bacteria can exploit a flagellar buckling instability to change direction," *Nat. Phys.*, vol. 9, no. 8, pp. 494–498, 2013.
- [4] M. L. Smith, G. M. Yanega, and A. Ruina, "Elastic instability model of rapid beak closure in hummingbirds," *J. Theor. Biol.*, vol. 282, no. 1, pp. 41–51, 2011.
- [5] L. Mahadevan and S. Rica, "Self-Organized Origami," vol. 307, no. March 2005, 2008.
- [6] B. Kresling, "Origami-structures in nature: lessons in designing 'smart' materials," *Mater. Res. Soc. Symp. Proc. Vol.*, vol. 1420, pp. 25–31, 2012.
- [7] J. L. Silverberg, A. A. Evans, L. McLeod, R. C. Hayward, T. Hull, C. D. Santangelo, and I. Cohen, "Applied origami. Using origami design principles to fold reprogrammable mechanical metamaterials.," *Science*, vol. 345, no. 6197, pp. 647–50, 2014.
- [8] J. L. Silverberg, J.-H. Na, A. A. Evans, B. Liu, T. C. Hull, C. D. Santangelo, R. J. Lang, R. C. Hayward, and I. Cohen, "Origami structures with a critical transition to bistability arising from hidden degrees of freedom.," *Nat. Mater.*, vol. 14, no. 4, pp. 389–393, 2015.
- [9] C. D. Onal, R. J. Wood, and D. Rus, "An origamiinspired approach to worm robots," *IEEE/ASME Trans. Mechatronics*, vol. 18, no. 2, pp. 430–438, 2013.
- [10] S. Felton, M. Tolley, E. Demaine, D. Rus, and R. Wood, "A method for building self-folding machines," *Science* (80-.)., vol. 345, no. 6197, pp. 644–646, 2014.
- [11] S. Miyashita, S. Guitron, M. Ludersdorfer, C. R. Sung, and D. Rus, "An untethered miniature origami robot that self-folds, walks, swims, and degrades," *2015 IEEE Int. Conf. Robot. Autom.*, pp. 1490–1496, 2015.
- [12] Z. Zhakypov, M. Falahi, M. Shah, and J. Paik, "The Design and Control of the Multi-Modal Locomotion Origami Robot, Tribot," pp. 4349–4355, 2015.
- [13] N. Nayakanti, S. Tawfick, and A. J. Hart, "Twist-coupled Kirigami Metamaterials and Mechanisms," *Prep.*, 2016.
- [14] C. Jianguo, M. Ruijun, Jian, Feng, Ya, Zhou, and D. Xiaowei, "Foldability Analysis of Cylindrical Origami Structures," *ReMar*, vol. 1, no. 36, 2016.
- [15] M. Schenk and S. D. Guest, "Geometry of Miura-folded metamaterials," *Proc. Natl. Acad. Sci.*, vol. 110, no. 9, pp. 3276–3281, 2013.